



## Effect of damage-related microstructural parameters on plate tearing at steady state

Tekogŕu, C.; Nielsen, K. L.

*Published in:*  
European Journal of Mechanics, A/Solids

*Link to article, DOI:*  
[10.1016/j.euromechsol.2019.103818](https://doi.org/10.1016/j.euromechsol.2019.103818)

*Publication date:*  
2019

*Document Version*  
Peer reviewed version

[Link back to DTU Orbit](#)

*Citation (APA):*  
Tekogŕu, C., & Nielsen, K. L. (2019). Effect of damage-related microstructural parameters on plate tearing at steady state. *European Journal of Mechanics, A/Solids*, 77, Article 103818. <https://doi.org/10.1016/j.euromechsol.2019.103818>

---

### General rights

Copyright and moral rights for the publications made accessible in the public portal are retained by the authors and/or other copyright owners and it is a condition of accessing publications that users recognise and abide by the legal requirements associated with these rights.

- Users may download and print one copy of any publication from the public portal for the purpose of private study or research.
- You may not further distribute the material or use it for any profit-making activity or commercial gain
- You may freely distribute the URL identifying the publication in the public portal

If you believe that this document breaches copyright please contact us providing details, and we will remove access to the work immediately and investigate your claim.

# Effect of Damage-Related Microstructural Parameters on Plate Tearing at Steady State

C. Tekoğlu<sup>a,\*</sup>, K.L. Nielsen<sup>b</sup>

<sup>a</sup>*Department of Mechanical Engineering, TOBB University of Economics and Technology, Söğütözü, Ankara, 06560, Turkey*

<sup>b</sup>*Department of Mechanical Engineering, Solid Mechanics, Technical University of Denmark, DK-2800 Kgs. Lyngby, Denmark*

---

## Abstract

The tearing of ductile metal plates can take place in three distinctly different modes: cup-cup, cup-cone, and crack slanting, but they are often observed in combination. It is well established that all tearing modes are governed by nucleation, growth, and coalescence of voids at the micron scale. What controls the shift between different tearing modes is, however, unclear and a micro-mechanics-based investigation is launched here to shed light on the issue. The present work takes as a starting point the hypothesis that the volume fraction, (average) size, and distribution of second phase particles, which act as void nucleation sites, are the key microstructural parameters that determine the tearing mode. In accordance with this hypothesis, the plates are modeled here by embedding randomly distributed void nucleation sites in a homogeneous matrix material. A parameter study is performed, and by adjusting the number, size and distribution of the nucleation sites in the fracture process zone, a shift in the tearing mode is achieved: a low number of small (relative to the plate thickness) randomly distributed particles link up in a void-by-void-type failure, whereas bigger particles, or a large number of small particles, can facilitate multiple void interactions. The present work also demonstrates that, for plates with intermediate or low volume fraction of nucleation sites, the localization of deformation in a macroscopic band precedes the microscopic localization that eventually links the voids. However, the two modes of plastic flow localization occur simultaneously for large volume fractions.

*Keywords:* Ductile failure, Gurson model, Shear band, Void coalescence, Finite element method

---

\*Corresponding author. Tel.:+90 312 292 42 29 ; fax:+90 312 292 40 91.

URL: [cihantekoglu@etu.edu.tr](mailto:cihantekoglu@etu.edu.tr); [c.tekoglu@gmail.com](mailto:c.tekoglu@gmail.com) (C. Tekoğlu)  
Preprint submitted to Elsevier

## 30 1. Introduction

31 Intermetallic inclusions are often deemed responsible for the nucleation of the micro-  
32 voids that, upon loading, grow to coalesce and eventually form the micro-cracks leading  
33 to material separation in ductile plate tearing. Distinct crack surface morphologies such  
34 as slanting, cup-cup, and cup-cone are observed for extensive crack growth in metal  
35 plates; see Fig. 1. The nucleation, growth, and coalescence of voids have been studied  
36 in great detail, and with the increasing computational resources, the chain of events  
37 are now being linked in ever more complex numerical analyses (see e.g. the reviews by  
38 Tvergaard, 1990; Benzerga and Leblond, 2010, and the references therein). An under-  
39 standing of the interplay between different mechanisms and length scales is, however,  
40 still in a maturing stage and key details remain to be unraveled and exploited for the  
41 creation of new and better materials. It is reported in the literature that plates fab-  
42 ricated from high-strength age-hardened aluminum alloys (Irwin et al., 1958; Knott,  
43 1973; Li and Siegmund, 2002), and high-strength steels (Broek, 1986) exhibit slanted  
44 crack growth, while plates fabricated from low-strength metals such as stainless steel,  
45 mild steel, 6082-O and NS4 aluminum alloys, brass, bronze, lead, and zinc systemati-  
46 cally show a cup-cup fracture profile (Pardoen et al., 2004), for several different plate  
47 thicknesses. Despite this insight, the transition between the tearing modes remains to  
48 be fully understood, and nowhere is a conclusive answer found to the question: *why*  
49 *does a propagating crack choose one tearing mode over the others?*

50 The current approach to ductile plate tearing in the literature, based on Gurson-like  
51 porous plasticity finite element (FE) models with a homogeneous material distribution  
52 in the entire fracture process zone (FPZ), cannot provide an unambiguous answer to  
53 the above question. For a sufficiently fine discretized plate with a homogenized porosity  
54 distribution, the crack propagates in a  $45^\circ$  orientated shear band for a wide range of  
55 material properties (Mathur et al., 1996; Felter and Nielsen, 2017; Andersen et al.,  
56 2018a). In fact, lowering the initial porosity and/or increasing the hardening capacity  
57 of the plate material while keeping the mesh unchanged can lead to a shift from slant  
58 to flat crack propagation. However, this shift is merely an artifact of the discretization;  
59 often one can make the crack slant again upon further mesh refinement. Besson et al.  
60 (2003) presented a detailed 2D study on the effect of discretization, and demonstrated

61 that the mesh type has a great influence on the Gurson model’s ability to describe  
62 slant crack propagation (see also Nielsen and Hutchinson, 2012).

63 It is well established that void nucleation becomes more and more difficult with  
64 decreasing second phase particle size (e.g Gurland, 1972; Lewandowski et al., 1989;  
65 Dighe et al., 2002), and that the presence of different families of particles with different  
66 sizes and/or void nucleation resistances have profound effects on void nucleation (e.g  
67 Marino et al., 1985; Bron et al., 2004; Asserin-Lebert et al., 2005). In the present work,  
68 the non-homogeneous distribution of the damage related microstructure is accounted  
69 for in terms of the spatial distribution, number and size of second phase particles,  
70 i.e. the void nucleation sites. The hypothesis is that a large number of closely packed  
71 nucleation sites will facilitate multiple void interaction, whereas fewer nucleation sites  
72 will link up in a void-by-void fashion. Therefore, changing the spatial distribution,  
73 number and/or size of the void nucleation sites in a metal plate, while keeping all  
74 other mechanical properties and loading conditions unchanged, is expected to lead  
75 to a change in the fracture surface morphology. Related to this is the discussion on  
76 the sequence of localized deformations at different length scales (also introduced in  
77 Tekoğlu et al., 2015). One important finding of the present paper is that, macroscopic  
78 band formation does not necessarily occur simultaneously with, but it can precede,  
79 microscopic localization at stress triaxialities below 1, unlike the conclusions arrived at  
80 in Tekoğlu et al. (2015).

81 The paper is structured as follows. The problem formulation and modeling assump-  
82 tions are laid out in Section 2, and the numerical methods are presented in Section 3.  
83 Results are given in Section 4, which is followed by a discussion and concluding remarks  
84 in Section 5.

## 85 **2. Problem formulation**

86 The schematic in Fig. 2a shows a ductile plate that tears under mode I loading. The  
87 dimensions of the plate in the  $x_2x_3$ -plane are much larger than its thickness in the  
88  $x_1$ -direction,  $W$ . All the cross sections perpendicular to the crack growth direction (the  
89  $x_3$ -direction in Fig. 2a) experience the same deformation history at steady state, such  
90 that: (1) a local thinning first develops far ahead of the crack tip, while the regions out-

91 side the thinning zone unload elastically, (2) the local thinning intensifies and damage  
 92 develops, (3) plastic deformation further localizes in deformation bands contained in  
 93 the local thinning region, and (4) a macro-crack propagates in the deformation bands  
 94 through coalescing voids, which finally leads to fracture of the cross section. The mode I  
 95 tearing problem considered here is similar to that investigated in Nielsen and Hutchin-  
 96 son (2012); Andersen et al. (2018b), where large-scale 3D steady-state plate tearing is  
 97 boiled down to an approximate 2D plane strain setup. The elastic unloading domain  
 98 above and below the thinning region essentially restricts the deformation in the FPZ  
 99 such that a plane strain condition can be assumed near the crack tip (an assumption  
 100 supported in a recent full 3D study by Andersen et al., 2018a). Thus, in the 2D plane  
 101 strain setup, a cross section in the  $x_1x_2$ -plane with an initial aspect ratio of  $H_0/W_0$   
 102 is imagined to be cut from the plate, and loaded in tension along the  $x_2$ -direction  
 103 to mimic a far-field mode I loading (see Fig. 2b). The difference in the present work  
 104 is that, rather than restricting the analysis to a homogeneous porous material as in  
 105 Nielsen and Hutchinson (2012); Morgeneyer et al. (2014); Andersen et al. (2018b), a  
 106 population of “discrete void nucleation sites” which represents the second phase parti-  
 107 cles in a real material, are embedded into the FPZ that evolves in the region specified  
 108 by its initial height,  $h_0$ , in Fig. 2b. The idea of modeling second phase particles as  
 109 void nucleation sites has been successfully implemented in the previous literature, see  
 110 e.g. Srivastava et al. (2014); Osovski et al. (2015); Morgeneyer et al. (2016); Srivastava  
 111 et al. (2017). The elastic unloading domain above and below the FPZ (the light gray  
 112 regions in Fig. 2b) is assumed to be non-porous and deforms by  $J_2$ -flow plasticity. In  
 113 this way, the adopted setup allows microstructural parameters such as the spatial dis-  
 114 tribution, number, and relative size (with respect to the plate thickness) of the second  
 115 phase particles to enter the analysis. In Fig. 2b, for example, the number of randomly  
 116 distributed void nucleation sites,  $N_p$ , is equal to 50 and all nucleation sites have the  
 117 same radius,  $R_p$ . A background porosity, which has been introduced to allow neigh-  
 118 boring sites to eventually coalesce, is allowed to nucleate between nucleation sites. In  
 119 this way, the background porosity represents a secondary population of particles with  
 120 a much smaller average size than the primary population located in the nucleation  
 121 sites, which is typical for metallic alloys. The Gurson—Tvergaard—Needleman (GTN)

122 porous plasticity model is employed to predict the porosity evolving from the void nu-  
 123 cleation sites as well as the macroscopic material separation that develops across the  
 124 plate thickness. The FE model corresponding to this 2D framework enables a compre-  
 125 hensive parameter study of the changes in the fracture surface morphology when the  
 126 damage related microstructural parameters are varied, see Section 3.

### 127 **3. Model: constitutive relations and finite element formulation**

128 The FE calculations in this paper are performed by using the commercial software  
 129 ABAQUS/Explicit, version 2016. In this section, the constitutive relations and the FE  
 130 formulation are only briefly introduced and the reader is referred to ABAQUS (2016)  
 131 for further details.

#### 132 *3.1. Constitutive relations*

133 Nucleation, growth, and coalescence of voids in the FPZ are accounted for by the  
 134 GTN porous plasticity model (see e.g. Tvergaard, 1981), which is based on the pio-  
 135 neering work of Gurson (1977). In the notation of ABAQUS, the yield surface for the  
 136 GTN model is given by:

$$\Phi = \left( \frac{q}{\sigma_y} \right)^2 + 2q_1 f^* \cosh \left( -q_2 \frac{3p}{2\sigma_y} \right) - (1 + q_3 (f^*)^2) = 0.$$

137 Here,  $q$  is the effective von Mises stress for the Cauchy stresses;  $\sigma_y[\bar{\epsilon}_m^{pl}]$  is the yield  
 138 stress of the fully dense matrix material as a function of the equivalent plastic strain in  
 139 the matrix,  $\bar{\epsilon}_m^{pl}$ ; the hydrostatic pressure is  $p$ ; and  $q_1$ ,  $q_2$ , and  $q_3$  are fitting parameters  
 140 introduced by Tvergaard (1981). The three fitting parameters, respectively, account for  
 141 the interaction between voids, void shape changes, and the effect of stress triaxiality  
 142 on void growth during loading. Finally,  $f^*[f]$  is a function of the void volume fraction,  
 143  $f$ , and is given by:

$$f^* = \begin{cases} f & \text{if } f \leq f_c, \\ f_c + \frac{\bar{f}_F - f_c}{\bar{f}_F - f_c} (f - f_c) & \text{if } f_c < f < \bar{f}_F, \\ \bar{f}_F = \frac{q_1 + \sqrt{q_1^2 - q_3}}{q_3} & \text{if } f \geq \bar{f}_F, \end{cases}$$

144 where  $f_c$  and  $f_F$  are the two values of the void volume fraction that correspond to the  
 145 onset of void coalescence and to the total loss of stress carrying capacity at a material  
 146 point, respectively. Once all the material points in an element fail (with  $f \geq f_F$ ), the  
 147 element is automatically removed from the mesh by ABAQUS/Explicit (see Section 3.2  
 148 for details on the element formulation).

149 In the GTN model, the total change in the porosity,  $\dot{f}$ , equals the sum of the change  
 150 due to newly nucleating voids,  $\dot{f}_{\text{nucl}}$ , and that due to growth of the existing voids,  $\dot{f}_{\text{gr}}$ ,  
 151 such that:  $\dot{f} = \dot{f}_{\text{nucl}} + \dot{f}_{\text{gr}}$ . In ABAQUS/Explicit, void nucleation is strain controlled,  
 152  $\dot{f}_{\text{nucl}} = A[\bar{\varepsilon}_m^{\text{pl}}] \dot{\varepsilon}_m^{\text{pl}}$ , and the probability density function,  $A[\bar{\varepsilon}_m^{\text{pl}}]$ , represents a Gaussian  
 153 bell distribution for the nucleation strain:

$$A[\bar{\varepsilon}_m^{\text{pl}}] = \frac{f_N}{s_N \sqrt{2\pi}} \exp \left[ \frac{-1}{2} \left( \frac{\bar{\varepsilon}_m^{\text{pl}} - \varepsilon_N}{s_N} \right)^2 \right],$$

154 where  $\varepsilon_N$  and  $s_N$  are, respectively, the mean value and the standard deviation for the  
 155 distribution, and  $f_N$  is the total volume fraction of the nucleated voids. The assumption  
 156 of a Gaussian bell distribution for void nucleation indirectly accounts for the fact that  
 157 the critical strain for void nucleation is a function of the size, shape, and orientation  
 158 of the second phase particles giving birth to voids. The growth of existing voids occurs  
 159 through the (incompressible) plastic deformation of the surrounding matrix material,  
 160 and the void growth equation directly follows from the conservation of mass in the  
 161 matrix:  $\dot{f}_{\text{gr}} = (1 - f) \dot{\varepsilon}_{\text{kk}}^{\text{pl}}$ . For  $f^* = f = 0$ , the material is fully dense, and the GTN  
 162 yield surface is identical to the von Mises yield surface.

163 In the present study, it is assumed that the undamaged material, both in the matrix  
 164 and at the nucleation sites, follows a true stress-logarithmic strain power hardening  
 165 relationship described as:

$$\sigma = \begin{cases} E\varepsilon & \text{if } \varepsilon < \varepsilon_0 \\ \sigma_0 \left( \frac{\varepsilon}{\varepsilon_0} \right)^N & \text{if } \varepsilon \geq \varepsilon_0 \end{cases}$$

166 where  $\sigma_0$  is the initial yield stress,  $E$  is Young's modulus,  $N$  is the hardening exponent,  
 167 and  $\varepsilon_0 = \sigma_0/E$ .

168 *3.2. Finite element (FE) formulation*

169 The FE calculations are conducted using the commercial software ABAQUS/Explicit,  
 170 in a finite strain setting. Fig. 3 shows a typical FE mesh for the plate tearing problem  
 171 described in Section 2. Before applying the load, the aspect ratio of the plate section is  
 172  $H_0/W_0 = 4$  for all the calculations, where  $H_0$  is the initial height of the plate section and  
 173  $W_0$  the initial plate thickness. The domain specified by the initial height,  $h_0 = H_0/2$ ,  
 174 where the FPZ will evolve, is finely discretized by using square elements having a nor-  
 175 malized edge length of  $L_e/W_0 = 10^{-3}$ . The mesh size gradually increases outside the  
 176 FPZ, toward the top and bottom boundaries, where an unstructured mesh containing  
 177 both quadrilateral and triangular elements is accepted. In the domain of the FPZ, there  
 178 is a total of  $N_p$  void nucleation sites, two of which are visible in the magnified view  
 179 given in Fig. 3. The void nucleation sites have a circular shape with radius  $R_p = kL_e$ ,  
 180 where  $k$  is an integer assumed to be the same for all the nucleation sites in a plate.  
 181 It is assumed that the individual void nucleation sites are non-overlapping and do not  
 182 intersect the cross-section boundaries. The adopted fine mesh allows a large number of  
 183 non-overlapping void nucleation sites in this zone: for  $k \leq 9$ ,  $N_p = 100$  non-overlapping  
 184 nucleation sites can easily be randomly distributed. The quadrilateral elements in the  
 185 mesh, including those in the FPZ, are of type CPE4R (four-noded, bilinear, reduced  
 186 integration with hourglass control), while the triangular elements are of type CPE3  
 187 (three-noded, linear); see ABAQUS (2016) for detailed element properties.

188 The plate is assumed to be non-porous in the undeformed configuration, with uni-  
 189 form mechanical properties throughout, representing a typical aluminum alloy: Young’s  
 190 modulus,  $E = 70$  GPa; Poisson ratio,  $\nu = 0.3$ ; density,  $\rho = 2700$  kg/m<sup>3</sup>; initial yield  
 191 stress,  $\sigma_0 = 300$  MPa; and a power-law hardening exponent,  $N = 0.1$ . The elastic un-  
 192 loading regions above and below the FPZ are taken to remain non-porous during the  
 193 entire loading history, whereas two different sets of porous plasticity parameters are  
 194 required inside the FPZ: one for the void nucleation sites (superscript “ns”) and one  
 195 for the matrix (superscript “m”) surrounding them. In this study, all the parameters  
 196 in both sets are taken to be the same ( $\varepsilon_N^{\text{ns}} = \varepsilon_N^{\text{m}} = 10^{-2}$ ,  $s_N^{\text{ns}} = s_N^{\text{m}} = (1/3) \times 10^{-2}$ ,  
 197  $f_c^{\text{ns}} = f_c^{\text{m}} = 10^{-2}$ ,  $f_F^{\text{ns}} = f_F^{\text{m}} = 5 \times 10^{-2}$ ) except for the total volume fraction of the  
 198 nucleated voids,  $f_N^{\text{ns}} = 8 \times 10^{-3}$ ,  $f_N^{\text{m}} = 10^{-5}$ .

199 In the present work, the intention is not to enter the regime where the inertia  
200 effect will become important. Even so, the explicit (but not the implicit) solver of  
201 ABAQUS is used for two reasons: i) it automatically removes failed elements and  
202 allows the simulation to represent the separation of the plate cross section, and ii) the  
203 dynamics helps to stabilize element failure, and by exploiting mass lumping (HRZ),  
204 the calculations are easily parallelized. The price to pay for these advantages is that  
205 great care must be taken to perform the analyses at sufficiently low deformation rates  
206 that the model response can be considered quasi-static. It is, here, worth mentioning  
207 that even for very low deformation rates, such convergence has been hard to achieve  
208 for some of the microstructures considered; for convergence, the kinetic energy in the  
209 system has to be much lower than the traditional 10% of the total energy in the system.  
210 In fact, the material parameters as well as the mesh size introduced above are chosen in  
211 a such way that they allow distinguishing between different crack surface morphologies,  
212 while the total CPU time of one FE calculation for a single plate is less than 24 hours.  
213 The FE calculations are performed on an HP Z420 workstation, running four central  
214 processing units in parallel. The effect of material parameters on the results is further  
215 discussed in Section 5.

## 216 4. Results

217 The main goal of this study is to investigate the effects of the spatial distribution,  
218 number,  $N_p$ , and the relative size,  $R_p = kL_e$ , of the second phase particles (acting as  
219 void nucleation sites) in relation to the fracture surface morphologies observed in plate  
220 tearing. The intervals for these key parameters, considered in the FE calculations, are:  
221  $N_p \in \{10, 25, 50, 75, 100\}$  and  $k \in \{3, 6, 9, 15, 18\}$ , while all other material and geo-  
222 metrical parameters remain fixed. All possible  $N_p - k$  combinations are analyzed, and  
223 three realizations with different spatial distributions of nucleation sites are considered  
224 for each combination (in all 75 FE calculations are conducted). The results are pre-  
225 sented below, by starting first with the detailed results for the two extreme cases with  
226  $N_p = 10, k = 3$  (Figs. 4–5) and  $N_p = 100, k = 18$  (Figs. 6–7), for which the frac-  
227 ture surface morphologies are distinctly apart. Attention is hereafter focused on the  
228 transition between the different fracture surface morphologies (Figs. 8-11).

229 Figure 4 shows the distribution of the void volume fraction in the FPZ at different  
 230 stages of the deformation history (Figs. 4a-d), together with the corresponding curve of  
 231 engineering stress versus engineering strain (Fig. 4e), for a plate with  $N_p = 10, k = 3$ .  
 232 The engineering stress is simply calculated by dividing the total reaction force in the  $x_2$ -  
 233 direction at the top (or bottom) boundary by the initial surface area,  $\Sigma_{22} = \sum_{i=1}^n (F_2^i/W_0)$ ,  
 234 while the ratio between the prescribed displacement at the boundary and the initial  
 235 height of the plate section gives the engineering strain,  $E_{22} = \Delta H/H_0$ . The asterisk (\*)  
 236 symbols on the stress-strain curve in Fig. 4e indicate the deformation stages depicted in  
 237 Figs. 4a-d. The onset of void nucleation coincides with the onset of plastic deformation,  
 238 and nucleation starts simultaneously at all nucleation sites in the FPZ. The void volume  
 239 fraction rapidly develops at the nucleation sites and the total amount is already two  
 240 orders of magnitude larger in the nucleation sites compared to the background porosity  
 241 of the surrounding matrix material at the very first plastic strain increment. Upon  
 242 further loading, the peak load is reached and diffuse thinning starts (see Fig. 4a). The  
 243 void volume fraction of all the nucleation sites subsequently intensifies as the thinning  
 244 develops, leading to failure through void coalescence at the length scale of elements.  
 245 The diffuse thinning is at some point interrupted by localization of deformation in two  
 246 roughly  $45^\circ$  shear bands reaching out from a single nucleation site located in the neck  
 247 (see Fig. 4b)<sup>1</sup>. It is noteworthy that the nucleation sites appear as discrete holes after  
 248 removing the failed elements from the mesh. A comparison of Figs. 4b—d reveals that  
 249 only the nucleation site, from which the shear bands emanate, enlarges after the onset  
 250 of localized deformation, while the development of the other nucleation sites (nearly)  
 251 stops. This is tied to the elastic unloading taking place outside the localization bands.  
 252 The fracture surface morphology thus largely resembles the cup-cup mode as the top  
 253 and bottom half plates no longer fit together. In fact, this observation is consistent for  
 254 different realizations of randomly distributed void nucleation sites (see Fig. 5).

255 Figure 5 shows the void volume fraction for two additional realizations of randomly  
 256 distributed void nucleation sites (plate P2 in Fig. 5b and plate P3 in Fig. 5c). Here, all

---

<sup>1</sup>Throughout the results, attention is focused on the developed void volume fraction as this is a clear indicator of plastic flow localization in the current model setup, see Appendix.

257 material parameters are kept constant and  $N_p = 10$ ,  $k = 3$ . The deformation and the  
258 complex sequence of events leading to fracture for P2 and P3 are the same as for P1;  
259 thinning is visible for all three plates, and they all have a cup-cup-like fracture surface  
260 morphology. The main difference in the fracture process of the three plates appear to  
261 be that, unlike in P1, the crack developed through more than one nucleation site in  
262 P2 and P3. However, the stress-strain curves for the three plates largely overlap until  
263 the onset of localized deformation (indicated by an asterisk (\*) in Fig. 5c), and even  
264 the onset of localized deformation matches up for P1 and P3. In contrast, P2 falls  
265 short of reaching the overall strain predicted for P1 and P3, but this is tied to the less  
266 pronounced development of the necking region.

267 Detailed results for the extreme case of a large number of big void nucleation sites  
268 ( $N_p = 100$  and  $k = 18$ ) are presented in Fig. 6. As in any other case analyzed, the  
269 void nucleation starts at the onset of plastic deformation. However, in contrast to the  
270 case of a few small void nucleation sites ( $N_p = 10$ ,  $k = 3$ ), the deformation quickly  
271 localizes in a macroscopic shear band at the onset of thinning, connecting multiple  
272 nucleation sites (see Fig. 6a). The tearing crack thereby propagates through the failure  
273 of the elements located in the most energetically favorable shear bands, and this leads  
274 to an overall slanted fracture surface morphology (see Fig. 6b). It is apparent from  
275 Fig. 7 that changing the realization of randomly distributed void nucleation sites while  
276 keeping all other material properties fixed (including  $N_p = 100$ ,  $k = 18$ ) does not affect  
277 the overall fracture surface morphology, although it shifts the location of the crack.  
278 Moreover, the stress-strain response is represented by (nearly) overlapping curves. In  
279 fact, the curves largely coincides with the response of P1 (with  $N_p = 10$ ,  $k = 3$ ) until  
280 the onset of localized deformation (see Fig. 7d).

281 Figure 8 shows the developed void volume fraction in the FPZ at the final step of  
282 fracture for four different plates all with small void nucleation sites ( $k = 3$ ), while the  
283 total numbers in each plate are  $N_p = 25$  (in Fig. 8a),  $N_p = 50$  (in Fig. 8b),  $N_p = 75$  (in  
284 Fig. 8c), and  $N_p = 100$  (in Fig. 8d), respectively. Considering the plates with  $N_p = 10$   
285 given in Fig. 5 as well, a gradual shift in the fracture surface morphology, first from  
286 cup-cup (Figs. 4, 5, and 8a) toward cup-cone (Figs. 8b and 8c), and later toward slanted  
287 (Fig. 8d) can be observed when increasing the number of randomly distributed void

288 nucleation sites. Companion results for four different plates with big void nucleation  
 289 sites ( $k = 18$ ) are shown in Fig. 9. Only the location of the crack is here shifted  
 290 by changing the random distribution, whereas all the plates display a slanted fracture  
 291 surface morphology. In fact, among 15 plates with  $k = 18$  and  $N_p \in \{10, 25, 50, 75, 100\}$   
 292 analyzed in this study, including those for which the results are not shown here, the  
 293 crack is predicted to be clearly slanted for 12, clearly cup-cone for 1, and a mixture of  
 294 the three morphologies for the remaining 2. It is also noteworthy that the amount of  
 295 diffuse thinning as well as the value of the macroscopic fracture strain decrease with  
 296 increasing  $N_p$ , for both  $k = 3$  and  $k = 18$ .

297 Additional results are presented in Figs. 10 and 11 to further clarify the effect of  
 298 the size of the void nucleation sites on the fracture surface morphology, by keeping the  
 299 realization of the random distribution the same for all the plates. The focus is kept on  
 300 the two extreme cases in terms of the number of nucleation sites, with  $N_p = 10$  for  
 301 Fig. 10 and  $N_p = 100$  for Fig. 11, while the size range is  $k \in [3, 6, 9, 15, 18]$ . For the  
 302 plates in Fig. 10 (Fig. 11), the spatial distribution of the nucleation sites is also the  
 303 same as the plate shown in Fig. 4 (Fig. 6). For  $k = 3$ , the fracture surface morphology  
 304 is of a cup-cup type both for  $N_p = 10$  (Fig. 4) and  $N_p = 100$  (Fig. 11a). For larger  
 305  $k$  values, the fracture surface morphology shifts to a cup-cone form for  $N_p = 10$ , and  
 306 the material separation takes place through the same set of interacting nucleation sites  
 307 (see Fig. 10). For  $N_p = 100$ , on the other hand, the fracture surface morphology shifts  
 308 to a slant-like form for small void nucleation sites and remains slanted thereafter (see  
 309 Fig. 11). As would be expected, the diffuse thinning region fades out and the fracture  
 310 strain decreases with increasing  $k$  for both  $N_p = 10$  and  $N_p = 100$ .

## 311 5. Discussion and Conclusions

312 The FE framework adopted in this study allows the effects of the size, number, and  
 313 spatial distribution of second phase particles to enter the analysis of ductile plate  
 314 tearing by embedding discrete void nucleation sites in the FPZ. The results show that  
 315 two local shear bands emanate from each void nucleation site as soon as the void volume  
 316 fraction in the nucleation site reaches approximately 0.1%. The two local shear bands  
 317 are perpendicular to each other, one aligned at  $45^\circ$  and the other at  $-45^\circ$  with respect

318 to the loading direction, and the plastic strain in the local shear bands is only slightly  
 319 larger than that in the surrounding matrix at this early stage of deformation; just  
 320 enough to make the shear bands apparent. Upon further monotonic loading, plasticity  
 321 increases everywhere in the plate, but intensifies the most in the local shear bands  
 322 spreading out from the void nucleation sites. At some point during the loading, an  
 323 interaction between the individual void nucleation sites sets in. The mechanism through  
 324 which this interaction takes place depends greatly on the size, number, and spatial  
 325 distribution of the nucleation sites, as well as on the porosity in the matrix surrounding  
 326 the sites.<sup>2</sup> The interaction mechanisms between void nucleation sites can be classified  
 327 into three distinct types: ① The existing local  $\pm 45^\circ$  shear bands spreading out from  
 328 several nucleation sites interact with one another in such a way as to form a global  
 329 localized deformation band extending over all these nucleation sites; see e.g. Fig. 6. ②  
 330 New shear bands form to connect neighboring void nucleation sites; see e.g. Figs. 12a  
 331 and 12b. This mechanism is also known as the “void sheeting mechanism”, where two  
 332 existing large voids are linked by a shear localization band in which new voids can  
 333 originate from secondary particles (see e.g. Cox and Low, 1974). ③ Neighboring void  
 334 nucleation sites merge with one another through local necking of the ligament situated  
 335 between them; see e.g. Figs. 12c and 12d.

336 Mechanism ① is active only if a macroscopic localization band can evolve due  
 337 to the interaction between the nucleation sites in the FPZ, and this is most likely  
 338 to be the case if the number or size (or both) of the void nucleation sites is large  
 339 enough. If active, mechanism ① sets in early in the deformation history, with no  
 340 or negligible diffuse thinning of the plate (see e.g. Fig. 7). In contrast, if the FPZ  
 341 contains only a few small void nucleation sites, a macroscopic localization band cannot  
 342 be achieved yielding a transient in the fracture surface morphology. In such plates,  
 343 the interaction between nucleation sites, if it ever takes place, is postponed until after  
 344 considerable diffuse thinning of the FPZ has developed. The plate shown in Fig. 4

---

<sup>2</sup>Note again that the background porosity in the matrix represents the presence of a secondary population of particles with much smaller sizes compared to the primary population of particles represented by the nucleation sites, see Section 2. In this study, the focus is on the primary population, and therefore the volume fraction of the secondary particles is assumed to be very small.

345 is a good example of the case where no interaction takes place between nucleation  
346 sites, and the crack spreads by the growth of a single nucleation site captured in  
347 the diffuse necking zone. A fracture process involving only a single void has recently  
348 been reported in an experimental study by Noell et al. (2018), for tensile testing of  
349 a sheet specimen fabricated from a high-purity (99.999 %) polycrystalline aluminum.  
350 Depending on the spatial distribution, however, more than one void nucleation site  
351 might be involved in crack propagation, joining together through mechanism (II) (see  
352 Figs. 5b and 5c). For intermediate levels of both the number and size of the void  
353 nucleation sites, even if there exists a  $45^\circ$  path extending over some nucleation sites,  
354 the path is usually not long enough to extend the entire plate thickness. The tearing  
355 crack can thereby propagate either through two intersecting global  $45^\circ$  shear bands,  
356 leading to a cup-cone morphology (see Fig. 8b), or by a combination of all three micro-  
357 mechanisms (see Fig. 8d). Clear examples of mechanism (III) are only observed between  
358 void nucleation sites located in close proximity, which reveals that the interaction  
359 between void nucleation sites in relation to plate tearing predominantly occurs via  
360 shear bands.

361 An issue that is closely related to the crack tearing mechanisms is the question of  
362 whether macroscopic localization occurs prior to microscopic localization, or whether  
363 the two occur simultaneously. In macroscopic localization, in either a normal band or a  
364 shear band, the softening giving rise to localized deformation is linked to the nucleation  
365 and growth of the voids. In microscopic localization, however, the softening is due to  
366 the coalescence of the voids where plastic strain is confined in the ligaments connecting  
367 neighboring voids. Tekoğlu et al. (2015) addressed this question by modeling an infinite  
368 planar band containing a doubly periodic array of initially spherical voids, embedded  
369 between two semi-infinite blocks of uniform, void-free material, in a three-dimensional  
370 FE setting. In Tekoğlu et al. (2015) it was concluded that; macroscopic localization  
371 precedes microscopic localization (or void coalescence) at stress triaxilities larger than  
372 1, as microscopic localization requires additional plastic straining in the deformation  
373 band. At lower stress triaxiality, however, the two modes of plastic flow localization  
374 occur simultaneously. In the present FE simulations of steady-state ductile tearing, the  
375 stress triaxiality is approximately 0.6 in the FPZ and it is clearly observed that macro-

376 scopic localization will precede microscopic localization. Only if failure takes place by  
377 the first mechanism, as discussed above, will the localized deformation in a macroscopic  
378 shear band occur simultaneously with the onset of void coalescence.<sup>3</sup> However, this is  
379 the case only when the number and/or size of the nucleation sites are large enough.  
380 For intermediate configurations of the damage related microstructure, macroscopic lo-  
381 calization precedes microscopic localization, which usually takes place through void  
382 sheeting (mechanism (II)), and rarely through coalescence of neighboring nucleation  
383 sites (mechanism (III)). With decreasing number and/or size of nucleation sites, the  
384 additional plastic straining in the localization band required to trigger microscopic lo-  
385 calization increases, and the separation between the two modes of localization becomes  
386 increasingly clear. As discussed in Tekoğlu et al. (2015), in their FE model: i) the voids  
387 are highly aligned, which possibly advances void coalescence, and ii) the outer blocks  
388 are void free, which postpones macroscopic localization; the combination of both ef-  
389 fects leads to simultaneous occurrence of the two modes at stress triaxialities below  
390 1. If these two restrictions are removed, as is the case for the present FE framework,  
391 macroscopic localization precedes microscopic localization even at triaxiality values as  
392 low as 0.6, except if the strain hardening capacity of the material is very low (in the  
393 present study, due to a large volume fraction of void nucleation sites).

394 In essence, what determines the fracture surface morphology is the strain hard-  
395 ening capacity of the plate material. This study emphasizes the fact that the strain  
396 hardening capacity of a material depends not only on the strain hardening exponent  
397 of the matrix, but also on the volume fraction and spatial distribution of the second  
398 phase particles, as well as on the ease of void nucleation at particle sites. Increasing  
399 the volume fraction of void nucleating particles would lower the hardening capacity of  
400 a material, the effect being more pronounced for easily void nucleating particles. The  
401 material parameters in this study are chosen in such a way to cover a broad spectrum

---

<sup>3</sup>It is worth noting that void coalescence within the elements inside a nucleation site, which occurs prior to macroscopic localization, is not the microscopic localization discussed here. The formation of a hole at a void nucleation site through coalescing voids simply mimics void nucleation at a particle, which, in reality, occurs either via brittle fracture of the particle, or the separation of the interface between the particle and the surrounding matrix.

402 of hardening capacities, by only changing the number,  $N_p$ , size,  $R_p$ , and spatial distri-  
403 bution of the void nucleation sites, while keeping the remaining parameters the same.  
404 At one end of the spectrum stand the plates with a low number of small nucleation  
405 sites, for which the hardening capacity is large and the crack predominantly propa-  
406 gates in a cup-cup morphology. At the other end are the plates with a large number of  
407 big nucleation sites, whose low hardening capacity forces the crack to slant. At these  
408 extremes of the spectrum, the crack profile depends mainly on the volume fraction of  
409 the nucleation sites; in the intermediate range, however, the spatial distribution is as  
410 important as the volume fraction.

411 The present study investigates only the effects of the size, number, and spatial  
412 distribution of second phase particles on the crack profile, while assuming all the re-  
413 maining mechanical and geometric parameters to be the same for all the cases analyzed.  
414 Employing, for example, a different set of material parameters could lead to a different  
415 fracture surface morphology for specific  $N_p - R_p$  combinations, especially for inter-  
416 mediate values. Although the general trends discussed above are expected to stand  
417 their ground, the mechanical properties of the matrix and the particles as well as the  
418 shape of the particles would affect when the transition from one crack morphology to  
419 another occurs. It will be, therefore, important to address this issue in the future. In  
420 fact, an attempt into this direction has been made in a recent work presented in Kaçar  
421 et al. (2017), which shows that the crack profile shifts from slanted to cup-cup with  
422 increasing matrix strain hardening capacity, in accordance with experiments.

423 Finally, it is worth noting that although the presented FE framework is suitable  
424 for the qualitative analyses performed in this study, a quantitative comparison with  
425 experiments would require a more advance ductile fracture model accounting for the  
426 effects of parameters such as void shape, anisotropic mechanical properties, kinematic  
427 hardening, etc.

## 428 **6. Acknowledgments**

429 The authors gratefully acknowledge the financial support by TÜBİTAK (Project No:  
430 315M133). KLN is financially supported by the VILLUM FOUNDATION Young In-  
431 vestigator Programme in the project “A New phenomenon Yet to be resolved in ductile

432 PLATE tearing”, grant VKR023451.

## 433 **References**

434 ABAQUS, 2016. Abaqus documentation collection, Version 2016, Providence, RI: Das-  
435 sault Systmes.

436 Andersen, R., Felter, C., Nielsen, K., 2018a. Micro-mechanics based cohesive zone mod-  
437 eling of full scale ductile plate tearing: from initiation to steady state. Submitted for  
438 publication.

439 Andersen, R., Woelke, P., Nielsen, K., 2018b. Cohesive traction-separation relations for  
440 plate tearing under mixed mode loading. *Eng. Frac. Mech.* 71, 199–209.

441 Asserin-Lebert, A., Besson, J., Gourgues, A. F., 2005. Fracture of 6056 aluminum sheet  
442 materials: effect of specimen thickness and hardening behavior on strain localization  
443 and toughness. *Materials Science and Engineering: A* 395, 186 – 194.

444 Benzerga, A. A., Leblond, J.-B., 2010. Ductile fracture by void growth to coalescence.  
445 *Adv. Appl. Mech.* 44, 169–305.

446 Besson, J., Steglich, D., Brocks, W., 2003. Modeling of plane strain ductile rupture.  
447 *Int. J. Plasticity* 19, 1517–1541.

448 Broek, D., 1986. *Elementary Engineering Fracture Mechanics*. Kluwer Academic Pub-  
449 lishers, Netherlands.

450 Bron, F., Besson, J., Pineau, A., 2004. Ductile rupture in thin sheets of two grades of  
451 2024 aluminum alloy. *Materials Science and Engineering: A* 380 (1), 356 – 364.

452 Cox, T. B., Low, J. R., 1974. An investigation of the plastic fracture of AISI 4340 and  
453 18 Nickel-200 grade maraging steels. *Metall. Trans.* 5 (6), 1457–1470.

454 Dighe, M. D., Gokhale, A. M., Horstemeyer, M. F., 2002. Second phase cracking and  
455 debonding observations in the fatigue damage evolution of a cast Al-Si-Mg alloy.  
456 *Metall. Mater. Trans* 33A, 1 – 8.

- 457 Felter, C. L., Nielsen, K. L., 2017. Assisted crack tip flipping under mode I thin sheet  
458 tearing. *Eur. J. Mech. A/Solids* 64, 58–68.
- 459 Gurland, J., 1972. Observations on the fracture of cementite particles in a spheroidized  
460 1.05% C steel deformed at room temperature. *Acta Metallurgica* 20, 735 – 741.
- 461 Gurson, A., 1977. Continuum theory of ductile rupture by void nucleation and growth  
462 - part I: yield criteria and flow rules for porous ductile media. *ASME J. Eng. Mater.*  
463 *Technol.* 99, 2–15.
- 464 Irwin, G. R., Kies, J. A., Smith, H. L., 1958. Fracture strengths relative to onset and  
465 arrest of crack propagation. In: *Proceedings of ASTM International*. Vol. 58. pp.  
466 640–60.
- 467 Kaçar, F., Tekoğlu, C., Nielsen, K. L., 2017. Fracture surface morphology under ductile  
468 tearing of metal plates. In: Høgsberg, J., Pedersen, N. L. (Eds.), *Proceedings of the*  
469 *30th Nordic Seminar on Computational Mechanics*, Kgs. Lyngby, Denmark. pp. 193  
470 – 196.
- 471 Knott, J. F., 1973. *Fundamentals of Fracture Mechanics*. Butterworths, London.
- 472 Lewandowski, J. J., Liu, C., Hunt, W. H., 1989. Effects of matrix microstructure and  
473 particle distribution on fracture of an aluminum metal matrix composite. *Materials*  
474 *Science and Engineering: A* 107, 241 – 255.
- 475 Li, W., Siegmund, T., 2002. An analysis of crack growth in thin-sheet metal via a  
476 cohesive zone model. *Engineering Fracture Mechanics* 69, 2073 – 2093.
- 477 Marino, B., Mudry, F., Pineau, A., 1985. Experimental study of cavity growth in ductile  
478 rupture. *Engineering Fracture Mechanics* 22, 989 – 996.
- 479 Mathur, K., Needleman, A., Tvergaard, V., 1996. Three dimensional analysis of dy-  
480 namic ductile crack growth in a thin plate. *J. Mech. Phys. Solids* 44 (3), 439–464.
- 481 Morgeneyer, T. F., Taillandier-Thomas, T., Buljac, A., Helfen, L., Hild, F., 2016. On  
482 strain and damage interactions during tearing: 3D in situ measurements and sim-

483     ulations for a ductile alloy (AA2139-T3). *Journal of the Mechanics and Physics of*  
484     *Solids* 96, 550 – 571.

485 Morgener, T. F., Taillandier-Thomas, T., Helfen, L., Baumbach, T., Sinclair, I.,  
486     Roux, S., Hild, F., 2014. In situ 3-D observation of early strain localization dur-  
487     ing failure of thin Al alloy (2198) sheet. *Acta Materialia* 69, 78 – 91.

488 Nielsen, K., Hutchinson, J., 2012. Cohesive traction-separation laws for tearing of duc-  
489     tile metal plates. *Int. J. Imp. Eng.* 48, 15–23.

490 Noell, P. J., Carroll, J. D., Boyce, B. L., 2018. The mechanisms of ductile rupture.  
491     *Acta Mater.* 161, 83 – 98.

492 Osovski, S., Srivastava, A., Ponson, L., Bouchaud, E., Tvergaard, V., Ravi-Chandar,  
493     K., Needleman, A., 2015. The effect of loading rate on ductile fracture toughness  
494     and fracture surface roughness. *J. Mech. Phys. Solids* 76, 20 – 46.

495 Pardoen, T., Hachez, F., Marchioni, B., Blyth, P. H., Atkins, A. G., 2004. Mode I  
496     fracture of sheet metal. *J. Mech. Phys. Solids* 52, 423 – 452.

497 Srivastava, A., Osovski, S., Needleman, A., 2017. Engineering the crack path by con-  
498     trolling the microstructure. *J. Mech. Phys. Solids* 100, 1 – 20.

499 Srivastava, A., Ponson, L., Osovski, S., Bouchaud, E., Tvergaard, V., Needleman, A.,  
500     2014. Effect of inclusion density on ductile fracture toughness and roughness. *J.*  
501     *Mech. Phys. Solids* 63, 62 – 79.

502 Tekoğlu, C., Hutchinson, J., Pardoen, T., 2015. On localization and void coalescence  
503     as a precursor to ductile fracture. *Phil. Trans. R. Soc.* A373.

504 Tvergaard, V., 1981. Influence of voids on shear band instabilities under plane strain  
505     condition. *Int. J. Fract. Mech.* 17, 389–407.

506 Tvergaard, V., 1990. Material failure by void growth to coalescence. *Adv. Appl. Mech*  
507     27, 83–151.

508 **Appendix**

509 Rather than considering the equivalent plastic strain, the evolution of damage is used  
 510 as an indicator of localization throughout the present work. This choice is motivated by  
 511 the fact that the localized deformation regions are clearly visible in both contour plots:  
 512 compare Figs. A-1a and A-1b, or Figs. A-1c and A-1d. All four figures correspond to the  
 513 onset of macroscopic localization, Figs. A-1a and A-1b for a plate with  $N_p = 10, k = 3$ ,  
 514 and Figs. A-1c and A-1d for a plate with  $N_p = 100, k = 18$ .

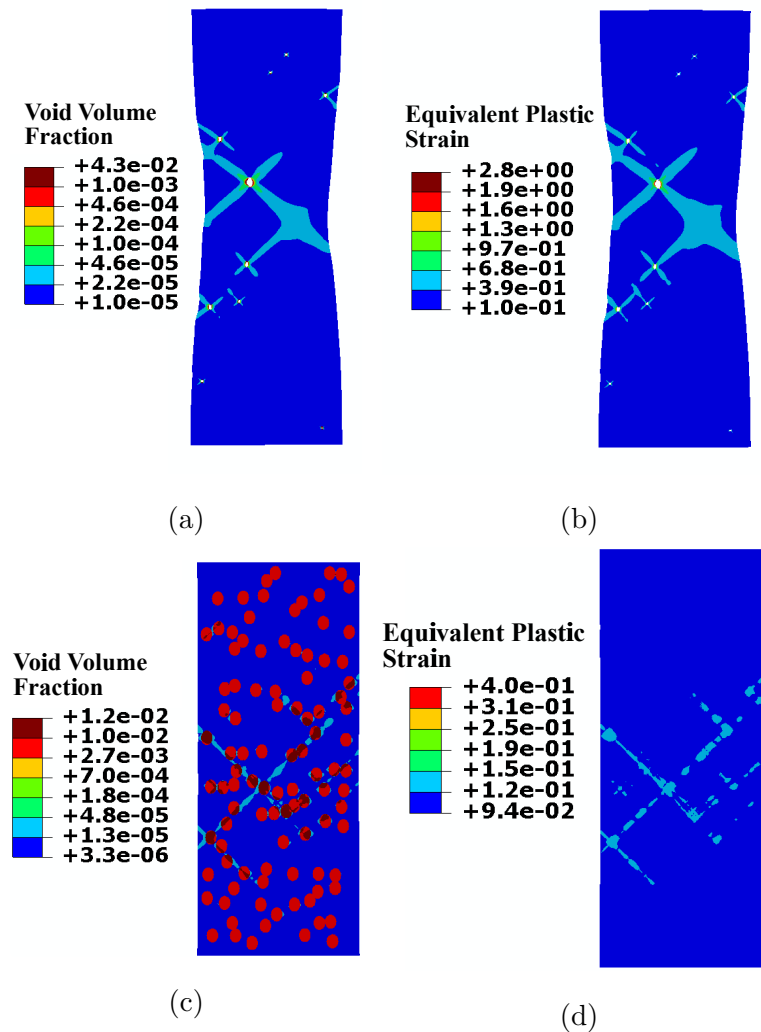


Figure A-1: Developed (a,c) void volume fraction and (b,d) equivalent plastic strain in the fracture process zone at the onset of macroscopic localization. The plate in (a,b), with  $N_p = 10, k = 3$ , is also shown in Fig. 4, and the plate in (c,d), with  $N_p = 100, k = 18$ , is also shown in Fig. 6.

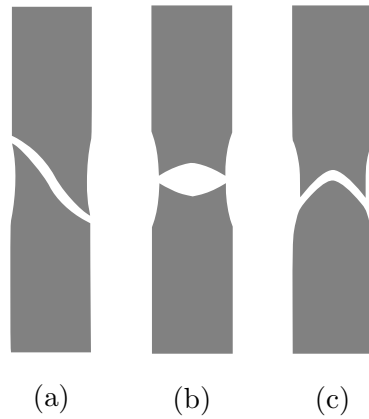


Figure 1: Schematic showing cross sections of cracked plate cross sections with the crack growing toward the reader: (a) the slanted crack growth, (b) the cup-cup crack growth (or bath tub), and (c) the cup-cone crack growth (or double slant).

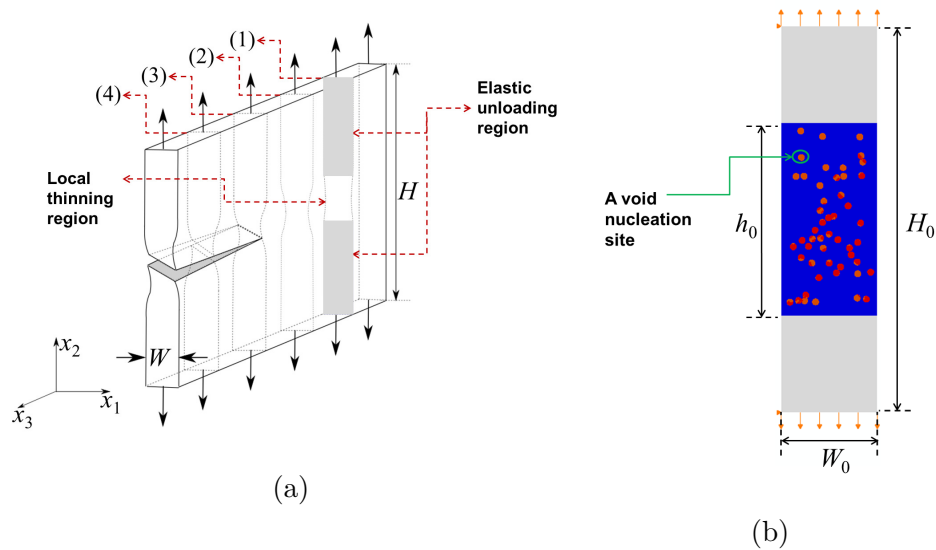


Figure 2: Schematic illustrating (a) a ductile plate under mode I loading, and (b) a 2D plane strain FE model for the plate in the undeformed configuration. Void nucleation sites in the fracture process zone (with a height of  $h_0$ ) represent the second phase particles in a real material.

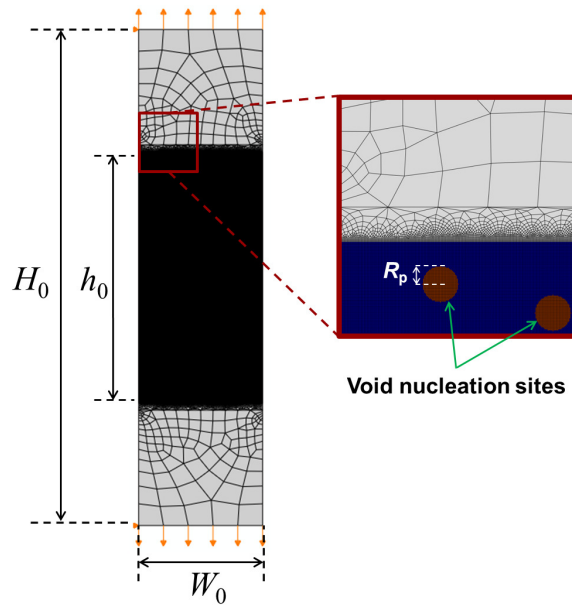


Figure 3: Schematic showing the boundary conditions and a typical mesh for the 2D plane strain FE model for a ductile plate under mode I loading. Void nucleation sites have an initial circular shape with a radius of  $R_p$ , as shown in the magnified view at the right. Mode I loading is imposed on the plate by pulling the top and bottom boundaries in the vertical direction, while letting them remain traction free in the horizontal direction. Moreover, the horizontal displacements of the two nodes located at the top-left and bottom-left corners are fixed, so that the top and bottom parts of the plate do not move in the horizontal direction with respect to one another once the crack starts to propagate.

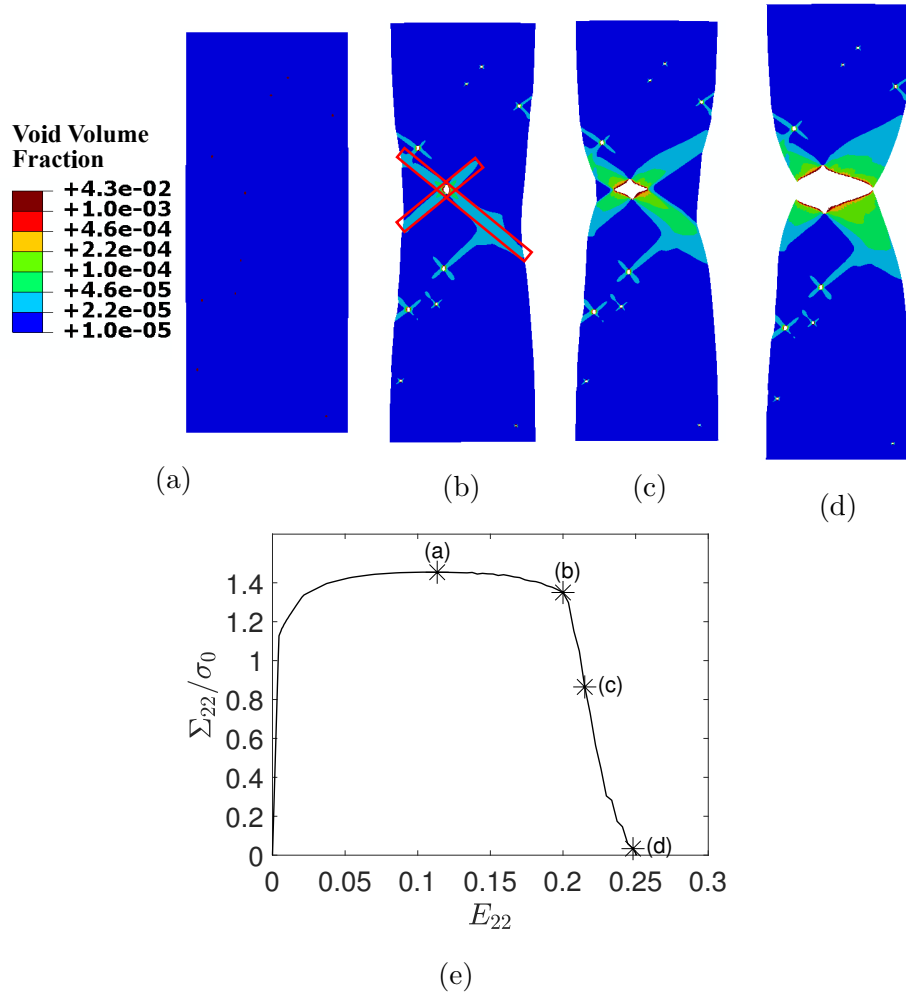


Figure 4: Developed void volume fraction in the fracture process zone for a plate with  $N_p = 10, k = 3$ , at (a) the onset of diffuse thinning, (b) the onset of macroscopic localization, (c) an intermediate deformation stage between the onset of macroscopic localization and final failure, and (d) the final failure. (e) Variation of the normalized engineering stress  $\Sigma_{22}/\sigma_0$  with the engineering strain  $E_{22}$  for the plate.

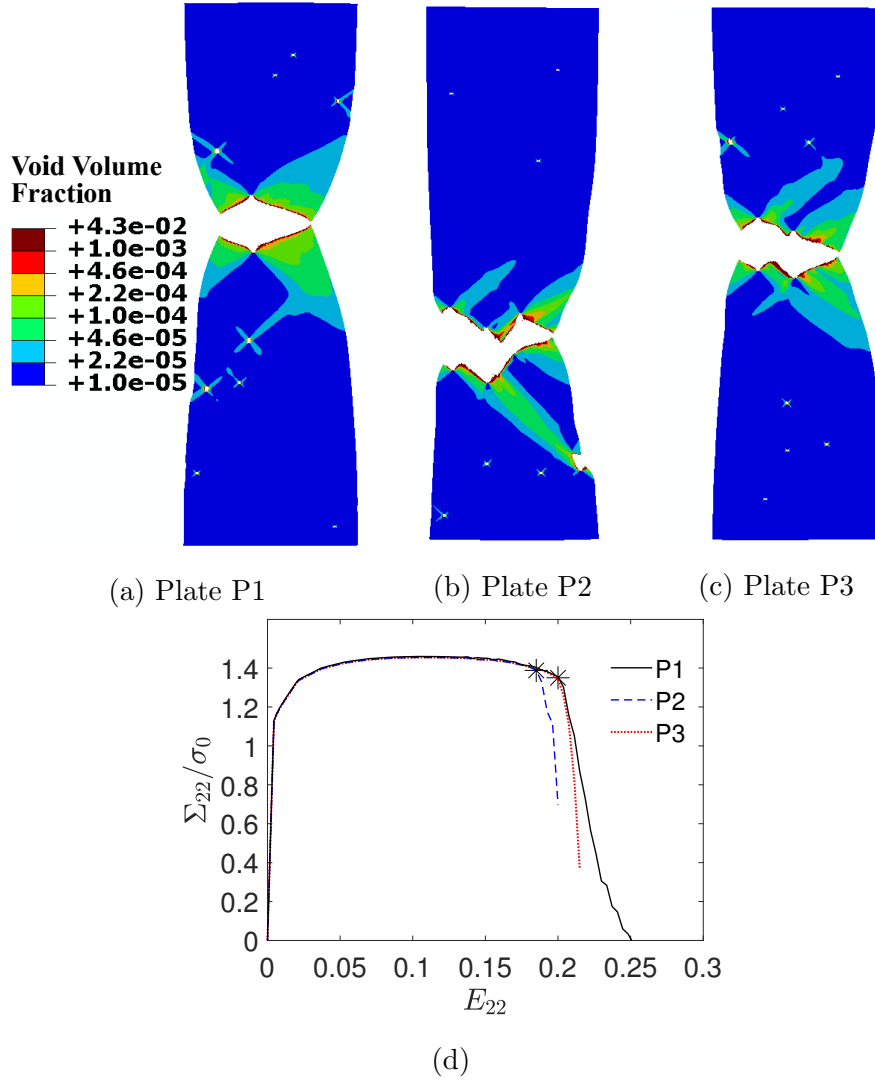


Figure 5: Developed void volume fraction in the fracture process zone for three plates with  $N_p = 10, k = 3$  at the final failure: (a) plate P1, (b) plate P2, and (c) plate P3. Plate P1 is also shown in Fig. 4. All the material parameters for these three plates are the same, the only difference being the realization of randomly distribution void nucleation sites. (d) Variation of the normalized engineering stress  $\Sigma_{22}/\sigma_0$  with the engineering strain  $E_{22}$  for the three plates.

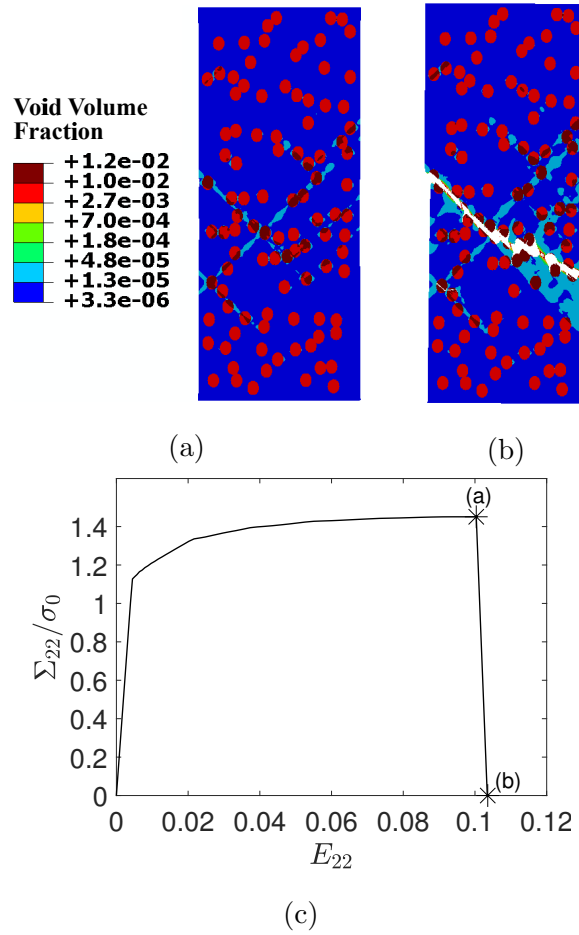


Figure 6: Developed void volume fraction in the fracture process zone for a plate with  $N_p = 100$ ,  $k = 18$  at the (a) onset of macroscopic localization, and (b) final failure. (c) Variation of the normalized engineering stress  $\Sigma_{22}/\sigma_0$  with the engineering strain  $E_{22}$  for the plate.

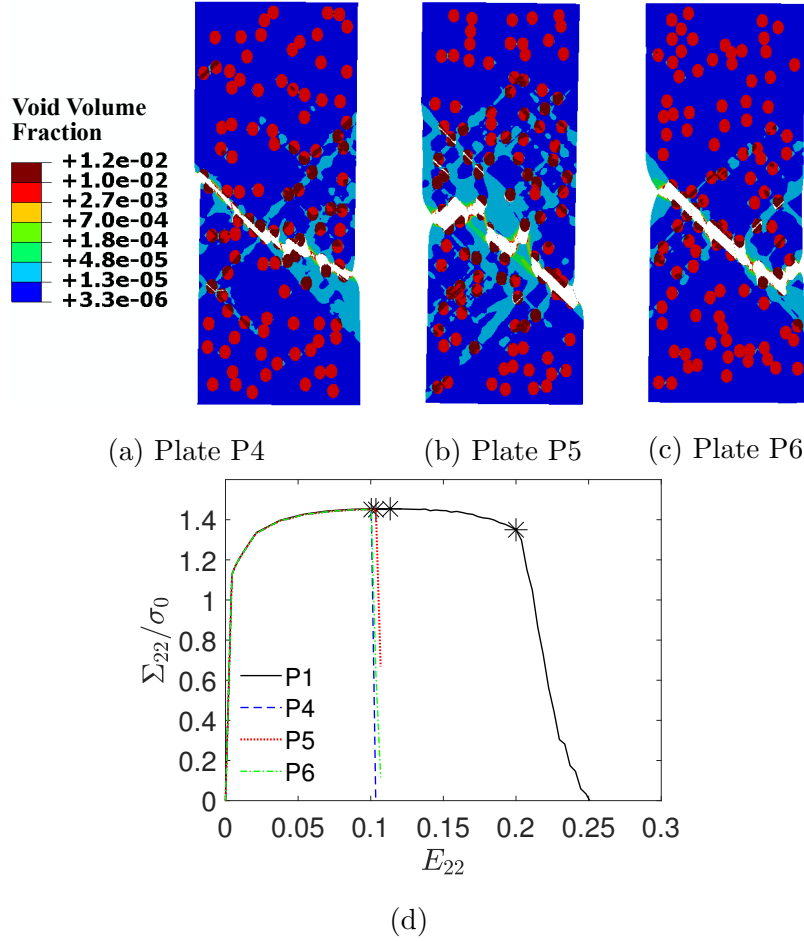


Figure 7: Developed void volume fraction in the fracture process zone for three plates with  $N_p = 100, k = 18$  at the final failure: (a) plate P4, (b) plate P5, and (c) plate P6. Plate P4 is also shown in Fig. 6. All the material parameters for these three plates are the same, the only difference being the spatial distribution of the void nucleation sites. (d) Variation of the normalized engineering stress  $\Sigma_{22}/\sigma_0$  with the engineering strain  $E_{22}$  for the plates P4, P5, P6 and the plate P1 (with  $N_p = 10, k = 3$ ) shown in Fig. 4.

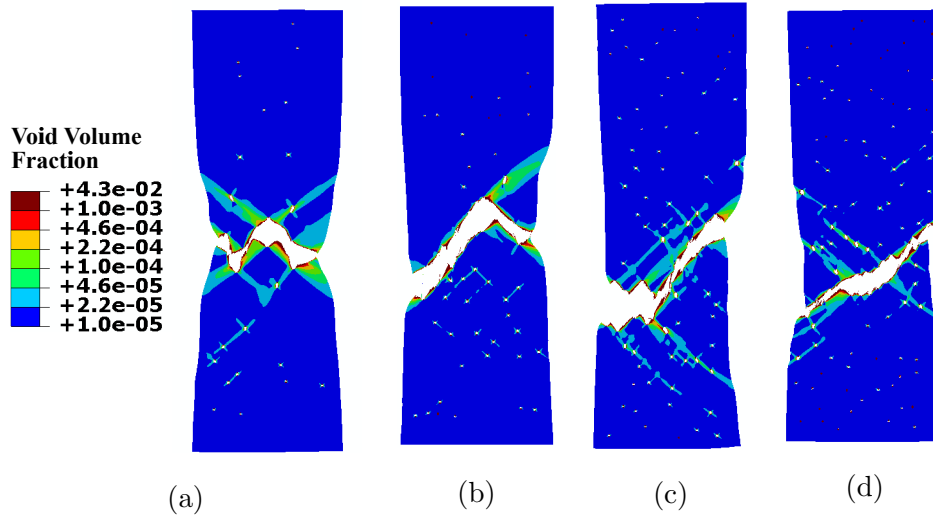


Figure 8: Developed void volume fraction in the fracture process zone for four different plates. The size of the void nucleation sites is the same for all the four plates ( $k = 3$ ), while their number is different: (a)  $N_p = 25$ , (b)  $N_p = 50$ , (c)  $N_p = 75$ , and (d)  $N_p = 100$ .

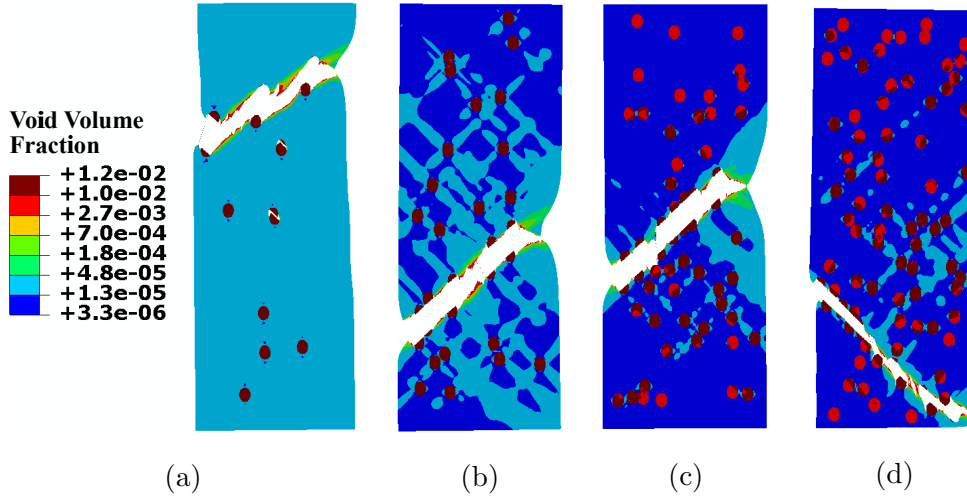


Figure 9: Developed void volume fraction in the fracture process zone for four different plates. The size of the void nucleation sites is the same for all the four plates ( $k = 18$ ), while their number is different: (a)  $N_p = 10$ , (b)  $N_p = 25$ , (c)  $N_p = 50$ , and (d)  $N_p = 75$ .

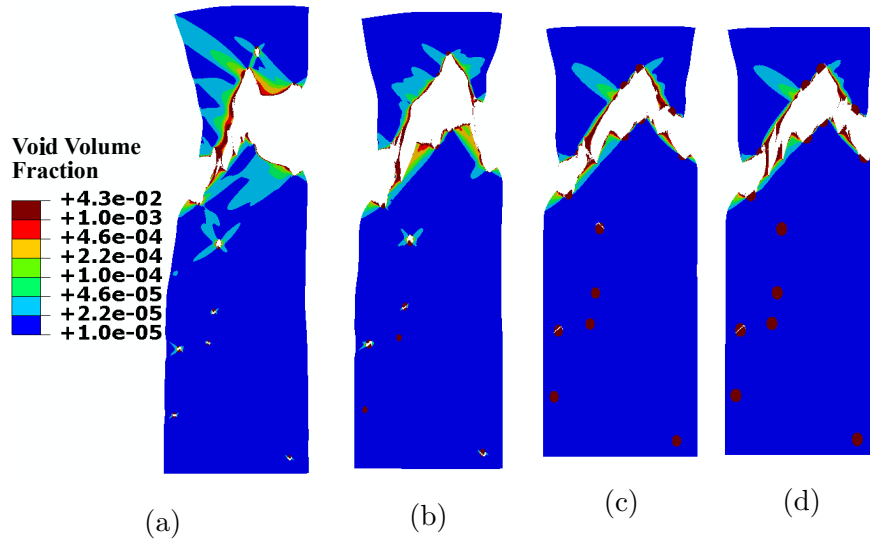


Figure 10: Developed void volume fraction in the fracture process zone for four different plates. The spatial distribution and the number of the void nucleation sites are the same for all the four plates ( $N_p = 10$ ), while their size is different: (a)  $k = 6$ , (b)  $k = 9$ , (c)  $k = 15$ , and (d)  $k = 18$ .

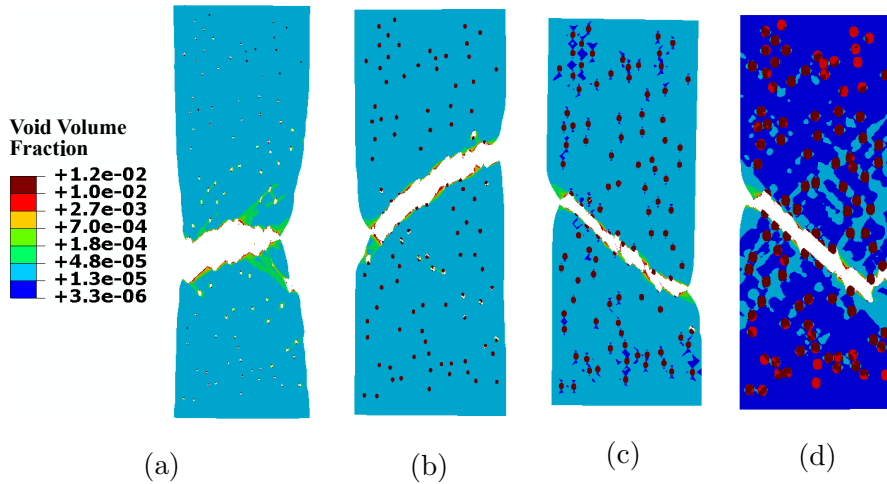


Figure 11: Developed void volume fraction in the fracture process zone for four different plates. The spatial distribution and the number of the void nucleation sites are the same for all the four plates ( $N_p = 100$ ), while their size is different: (a)  $k = 3$ , (b)  $k = 6$ , (c)  $k = 9$ , and (d)  $k = 15$ .

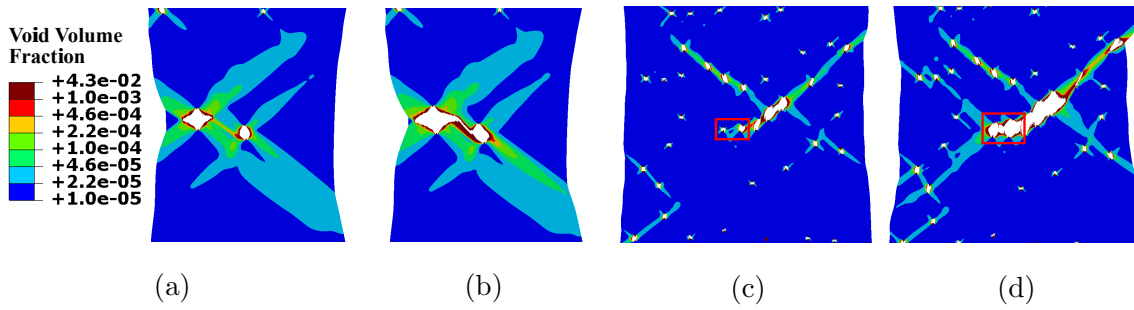


Figure 12: (a) Onset of void sheeting and (b) separation of the matrix through void sheeting between two void nucleation sites. (c) Onset of coalescence and (d) internal necking of the ligament between two void nucleation sites. The plate in (a,b) is also shown in Fig. 5c, and the one in (c,d) is also shown in Fig. 8d.